RELAXATION OSCILLATIONS IN TIDALLY EVOLVING SATELLITES

DANE QUINN[1], BRETT GLADMAN[2], PHIL NICHOLSON[2] and RICHARD RAND[3]
[1]*Department of Mechanical Engineering, The University of Akron, Akron, OH 44325-3903, U.S.A.*
e-mail: quinn@uakron.edu
[2]*Department of Astronomy, Cornell University, Ithaca, NY 14853, U.S.A.*
[3]*Department of Theoretical and Applied Mechanics, Cornell University, Ithaca, NY 14853, U.S.A.*

(Received: 13 August 1996; accepted: 26 February 1997)

Abstract. We study the rotational evolution under tidal torques of axisymmetric natural satellites in inclined, precessing orbits. In the spin- and orbit-averaged equations of motion, we find that a global limit cycle exists for parameter values near the stability limit of Cassini state $\mathcal{S}_1$. The limit cycle involves an alternation between states of near-synchronous spin at low obliquity, and strongly subsynchronous spin at an obliquity near 90°. This dynamical feature is characterized as a relaxation oscillation, arising as the system slowly traverses two saddle-node bifurcations in a reduced system. This slow time scale is controlled by ε, the nondimensional tidal dissipation rate. Unfortunately, a straightforward expansion of the governing equations for small ε is shown to be insufficient for understanding the underlying structure of the system. Rather, the dynamical equations of motion possess a singular term, multiplied by ε, which vanishes in the unperturbed system. We thus provide a demonstration that a dissipatively perturbed conservative system can behave qualitatively differently from the unperturbed system.

Key words: tidal despinning, limit cycles, Cassini states, relaxation oscillations, singular perturbations.

1. Introduction

The equilibrium configurations of a spinning, non-spherical satellite in an inclined, precessing orbit, or generalized Cassini states (Henrard and Murigande, 1987; Peale, 1969) have long been known. A rigorous treatment of the long-term stability of these states under the action of tidal torques has, however, been lacking. In a numerical analysis of the orbit- and spin-averaged equations of motion during the process of tidal despinning (Gladman et al., 1996), an axisymmetric satellite was found to exhibit limit-cycle behavior for certain values of the parameters. An exploration of the origin of this unexpected behavior, which occurs near the stability limit of Cassini state $\mathcal{S}_1$, forms the subject of this paper.

Consider a natural satellite in a circular orbit about a large planet, with the satellite orbit normal $\hat{\mathbf{K}}$ at an inclination i with respect to an invariable plane normal $\hat{\mathbf{n}}$. This invariable plane is generally taken to be the Laplace plane of the satellite in the sun-planet-satellite system. For inner satellites this is the equatorial plane of the planet while for outer satellites (such as the Moon), the Laplace plane is the ecliptic plane, i.e., the orbital plane of the planet about the sun. In addition, the orbit normal precesses about $\hat{\mathbf{n}}$ at a rate $-\mu$. This precession can be driven by the gravitational attraction of either a non-spherical planet or a third body (e.g., the Sun).

Celestial Mechanics and Dynamical Astronomy **67:** 111–130, 1997.

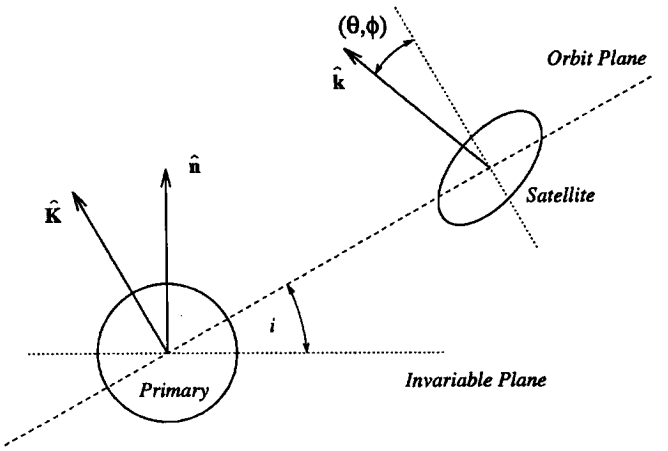

Figure 1. Satellite geometry. The satellite orbits in a plane with normal $\hat{\mathbf{K}}$, while this orbital plane regresses about the invariable plane normal $\hat{\mathbf{n}}$, at an angular rate $-\mu$. The obliquity θ of the satellite spin vector $\hat{\mathbf{k}}$ is measured with respect to the orbit normal. The variable ϕ is the azimuthal coordinate of $\hat{\mathbf{k}}$ with respect to the intersection of the orbit plane and the invariable plane. Applied torques cause the spin vector $\hat{\mathbf{k}}$ to precess about the orbit normal $\hat{\mathbf{K}}$.

We assume that the oblate satellite is axisymmetric and in a state of principal axis rotation about its axis of maximum moment of inertia, $\hat{\mathbf{k}}$. With respect to the orbit normal $\hat{\mathbf{K}}$, the spin angular momentum in the $\hat{\mathbf{k}}$ direction is located by the polar coordinates θ and ϕ, where $\theta \in (0, \pi)$ is referred to as the obliquity of the satellite and $\phi \in [0, 2\pi)$ is the azimuthal coordinate of $\hat{\mathbf{k}}$ with respect to the ascending node of the orbit plane of the satellite on the invariable plane (see Figure 1). Under the influence of tidal and solid-body torques, the following set of averaged, nondimensional equations of motion have been derived by Gladman et al., (1996):

$$\dot{\omega} = -\frac{\varepsilon}{2}\omega\left\{\cos^2\theta - 2\frac{\gamma}{\omega}\cos\theta + 1\right\}, \tag{1a}$$

$$\dot{\theta} = \sin i \sin\phi + \varepsilon \sin\theta\left\{\frac{\cos\theta}{2} - \frac{\gamma}{\omega}\right\}, \tag{1b}$$

$$\dot{\phi} = \sin i \frac{\cos\theta}{\sin\theta}\cos\phi + \cos i - \frac{\cos\theta}{\omega}, \tag{1c}$$

where $\omega \in (0, \infty)$, is the nondimensional rotational angular velocity of the satellite. In this nondimensional form, the time t is scaled by the orbital precession rate μ: $t = \mu\bar{t}$, while ω is scaled by the change in spin rate due to the torque exerted by the primary on the satellite's permanent deformation over one time unit:

$$\omega \equiv \frac{\bar{\omega}\mu}{S}.$$

Here, overbars refer to the corresponding dimensional quantities, and the quantity S is given by Gladman et al., (1996):

$$S = \frac{3Gm_p}{2r^3}\frac{C-A}{C},$$

where m_p is the mass of the primary, r is the radius of the satellite's (circular) orbit, and A and C are the satellite's equatorial and polar moments of inertia, respectively. The nondimensional spin rate corresponding to synchronous rotation (i.e., $\bar{\omega} = n$, the orbital mean motion) is denoted:

$$\gamma \equiv \frac{n\mu}{S} = \frac{2\mu}{3n}\left(\frac{C}{C-A}\right),$$

using Kepler's third law.

The equations of motion are written in a coordinate system fixed in the precessing orbit plane. In Equations (1) the terms dependent on the inclination of the orbit plane result from this rotating coordinate system. The external torques arise from the effect of the gravitational attraction between the point mass primary and the satellite. The solid-body torque results from the permanent oblateness of the satellite. Averaged over an orbital period, this quantity is $-SC\sin\theta\cos\theta$, and gives rise to the $\cos\theta/\omega$ term. The tidal torques result from a phase lag in the tidal deformation of the satellite and produce the $\mathcal{O}(\varepsilon)$ perturbations in the above system. The small parameter ε is the fractional amount by which the tides reduce the spin rate in one time unit, μ^{-1} (Gladman et al., 1996, Equation (56)).

In the following analysis, we will develop several simple approximations to this system. For this reason we will refer to Equations (1) as the original equations. We note that in Gladman et al. (1996), Equations (1) are referred to as the axisymmetric system.

In what follows, we will see that γ plays the key role in determining the character of the solutions to Equations (1). Noting that, for a synchronous satellite with small obliquity, the forced precession rate of the spin axis $\hat{\mathbf{k}}$ about the orbit normal $\hat{\mathbf{K}}$ is given by:

$$\begin{aligned}\dot{\Omega} &= -\frac{SC\sin\theta\cos\theta}{C\bar{\omega}\sin\theta},\\ &\simeq -\frac{S}{n} = -\frac{3n}{2}\left(\frac{C-A}{C}\right),\end{aligned}$$

and we see that for low obliquity, in physical terms, γ is simply the ratio of the orbital precession rate $-\mu$ to the synchronous spin axis precession rate $\dot{\Omega}$.

For most tidally-despun satellites, μ is controlled by the planet's gravitational quadrupole moment J_2, and hence:

$$\gamma_{\text{close}} \simeq J_2\left(\frac{r_p}{r}\right)^2\frac{C}{C-A},$$

where r_p is the equatorial radius of the planet. If, moreover, the satellite has a figure of oblate hydrostatic equilibrium, then:

$$\frac{C-A}{C} \simeq \frac{5}{4}\frac{\bar{\omega}^2 r_s^3}{G m_s},$$

and, setting $\bar{\omega} = n$, we have:

$$\gamma_{\text{close, hydro}} \simeq \frac{4}{5} J_2 \left(\frac{\rho_s}{\rho_p}\right)\left(\frac{r}{r_p}\right),$$

where ρ_s and ρ_p are the mean densities of the satellite and planet. For more distant satellites dominated by solar perturbations, $\mu \simeq (3/4)(n_p^2/n)$, where n_p is the planet's orbital mean motion. In this case we have:

$$\gamma_{\text{distant}} \simeq \frac{1}{2}\left(\frac{n_p}{n}\right)^2 \frac{C}{C-A} \propto r^3.$$

For known tidally-despun natural satellites, the nondimensional synchronous spin rate γ is generally in the range $10^{-4} - 10^{-2}$ (Gladman et al., 1996, Table II). This is due to the slow orbital precession rates of most satellites relative to their spin precession rates. The only known exception is that of the Moon, for which the large orbital radius and the small oblateness lead to $\gamma = 5.3259$.

With no tidal dissipation (so that $\varepsilon = 0$), the spin precession dynamics of the satellite are controlled by the spin rate ω, which, in this restricted system, is constant. Equations (1) possess either two or four equilibrium points, depending on whether ω is larger or smaller than a critical bifurcation value $\omega_{\text{cr}} \sim \mathcal{O}(1)$ (see Section 3). These equilibrium points are known as generalized Cassini states.

For $\gamma \gg \omega_{\text{cr}}$, Gladman et al. (1996), showed that the only possible stable endpoint for an axisymmetric satellite under the influence of tidal torques is state $\mathcal{S}_2$. For $\gamma \ll \omega_{\text{cr}}$, Cassini state $\mathcal{S}_1$ is the only possible endpoint for these equations. However, for $\gamma \sim \omega_{\text{cr}}$, more complex evolutionary scenarios can result, which are the subject of the present analysis.

Although this region of γ is unlikely to be occupied by any natural satellites at present, we note that energy loss associated with planetary tides can result in the very slow expansion of the orbit radius. One consequence of this evolution is a slowly increasing value of γ as the orbital radius increases, on timescales much longer than the evolution of the state variables considered here. The lunar value of γ was $\sim \omega_{\text{cr}}$ at an orbital radius of $\sim$ 34 Earth radii, at which time the Moon is thought to have transferred from Cassini state $\mathcal{S}_1$ to the present $\mathcal{S}_2$ state (Ward, 1975).

The value of the tidal dissipation parameter ε determines the absolute rate at which spin evolution proceeds, but, provided $\varepsilon \ll 1$, its numerical value is not important in controlling the nature of that evolution. For nominal values of

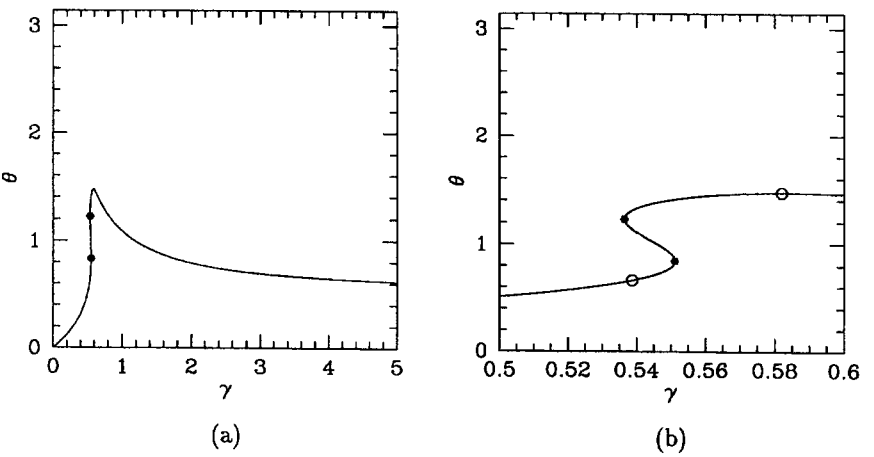

Figure 2. Bifurcation Diagram ($i = 30°$, $\varepsilon = 0.1$): the location of the equilibrium points in θ is shown as a function of the parameter γ. Figure (b) is a closeup of Figure (a). In each panel, two saddle-node bifurcations, corresponding to vertical tangencies on the branch of equilibria, are marked with filled points at $\gamma = 0.536$ and $\gamma = 0.551$. In Figure (b), the two Hopf bifurcations (marked by open circles) are also shown at $\gamma = 0.538$ and $\gamma = 0.582$. The Hopf bifurcations are not shown in Figure (a) because of the small range in γ over which these bifurcations occur.

elasticity and density, and for a tidal $Q = 100$, Gladman *et al.* (1996), estimated values of ε for the natural satellites in the range $10^{-6} - 10^{-2}$. The present lunar value is $\varepsilon_{\text{lunar}} = 2 \times 10^{-5}$, while the value at $34R_E$ was $\sim 6 \times 10^{-4}$. For most of the numerical calculations in the present work we have adopted a somewhat larger value of $\varepsilon = 0.1$, in order to speed up the tidal evolution and elucidate the numerical results.

2. A Global Limit Cycle

In Figure 2 we show a bifurcation diagram of Equations (1), for $\varepsilon = 0.1$ and $i = 30°$. For $0 < \gamma < 0.538$ and $\gamma > 0.582$, numerically we find that all solutions tend to a stable equilibrium point as suggested by Peale (1974). However, for $\gamma \in (0.538, 0.582)$, no stable fixed points exist and solutions are instead attracted to a global limit cycle. Note that the existence of the limit cycle, although related, does not directly correspond to the saddle-node bifurcations of the equilibria (as marked by filled points in Figure 2), which mark the limits of existence of Cassini states $\mathcal{S}_1$, $\mathcal{S}_4$, and $\mathcal{S}_2$. Instead, we find that the global limit cycle arises from Hopf bifurcations that occur at $\gamma = 0.538$ and $\gamma = 0.582$. An equilibrium point is said to undergo a Hopf bifurcation when two of its eigenvalues cross the imaginary axis, indicating a change in stability as some parameter is varied. Generically, such bifurcations are accompanied by the birth of a periodic orbit (Guckenheimer and Holmes, 1983; Hale and Koçak, 1991).

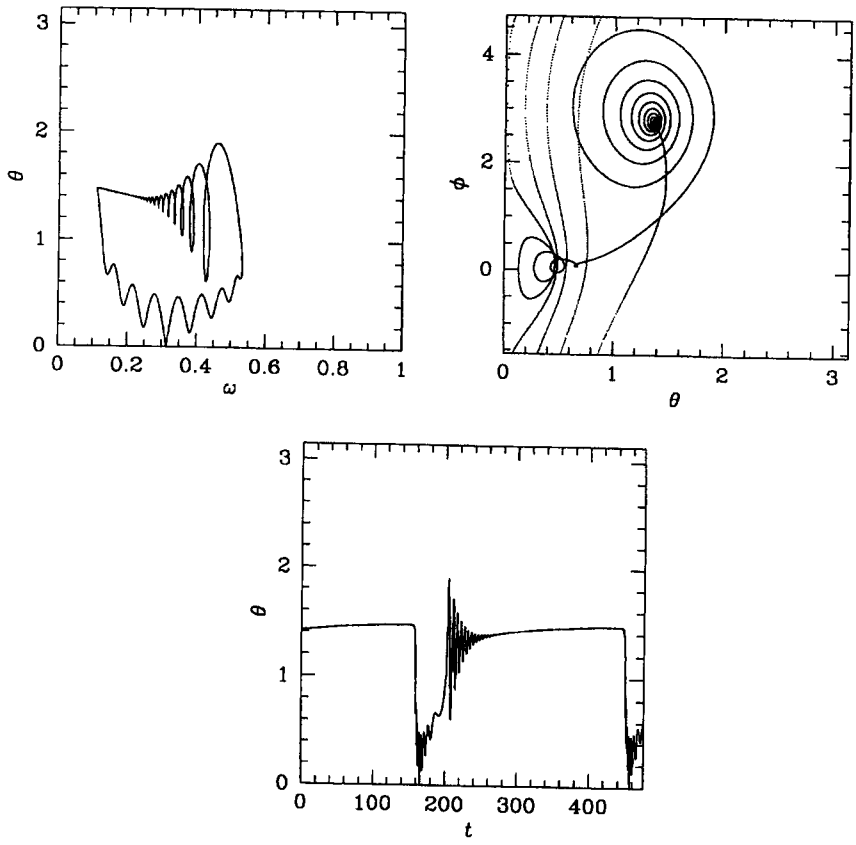

Figure 3. Globally stable limit cycle: $\gamma = 0.56$, $i = 30°$, and $\varepsilon = 0.1$.

In Figure 3 we show the global limit cycle that exists in Equations (1) for $\gamma = 0.56$, $i = 30°$, and $\varepsilon = 0.1$. The limit cycle is characteristically composed of two regions of damped oscillating motion connected by 'jumps'. Physically, the satellite spends a long time rotating sub-synchronously at high obliquity, before rapidly rolling over to low obliquity. During this traverse, the spin axis $\hat{\mathbf{k}}$ circulates around the orbit normal (in the integration this is seen as ϕ making four complete rotations through 2π). The satellite then wobbles around a low obliquity state for a relatively short time, while increasing its spin rate towards the synchronous value $\omega_{\text{syn}} = \gamma = 0.56$, before jumping back and damping to the slowly-varying high obliquity state (near $\theta = \pi/2$). This process repeats to create the limit cycle. This behavior can best be seen in the θ vs. t plot. We point out again that no known satellites *presently* occupy this intermediate range of γ. However, as the orbital radius of a satellite evolves, the accompanying value of γ could traverse this region in parameter space.

The spin evolution of triaxial satellites in circular orbits has been studied by Gladman et al. (1996). When the two equatorial moments of inertia are equal, the equations governing triaxial satellites reduce to Equations (1). However, under the action of tidal dissipation a triaxial satellite is found to asymptotically approach synchronous rotation, or $\omega = \gamma$, for all parameter values corresponding to known satellites. Effectively, the solid-body torque on the long axis stabilizes the orientation of the satellite relative to the planet, preventing subsynchronous rotation.

In this paper we attempt to understand the origin of the limit cycle for an axisymmetric satellite and the absence of a stable equilibrium point. Using geometrical techniques and the structure of a reduced system, we analyze the asymptotic behavior of this system.

3. Unperturbed System

We will treat ε, which characterizes the strength of the tidal damping, as a small parameter. In the $\varepsilon = 0$ limit the system is conservative and ω, the nondimensional spin rate, becomes constant. As a result, Equations (1) reduce to the one-degree-of-freedom system:

$$\dot{\omega} = 0, \tag{2a}$$

$$\dot{\theta} = \sin i \sin \phi, \tag{2b}$$

$$\dot{\phi} = \sin i \frac{\cos\theta}{\sin\theta} \cos\phi + \cos i - \frac{\cos\theta}{\omega}, \tag{2c}$$

which possesses the first integral:

$$\mathcal{H}(\theta, \phi) = \sin i \sin\theta \cos\phi - \cos i \cos\theta + \frac{\cos^2\theta}{2\omega}. \tag{3}$$

The equilibrium points of this system are defined as the generalized Cassini states (Peale, 1969).

In the $\varepsilon = 0$ limit, the unperturbed system is independent of the synchronous rotation rate γ. Rather, the spin rate is constant and ω becomes an additional parameter of the system. The equilibrium points of Equations (2) are found from Equation (2b) to satisfy $\sin\phi = 0$, so that:

$$\phi = 0 \quad \text{or} \quad \pi.$$

Substituting this into Equation (2c), equilibrium points must satisfy the following equation:

$$\sin(\theta + \xi i) - \frac{\sin 2\theta}{2\omega} = 0, \qquad \xi = \begin{cases} +1, & \text{if } \phi = 0, \\ -1, & \text{if } \phi = \pi. \end{cases} \tag{4}$$

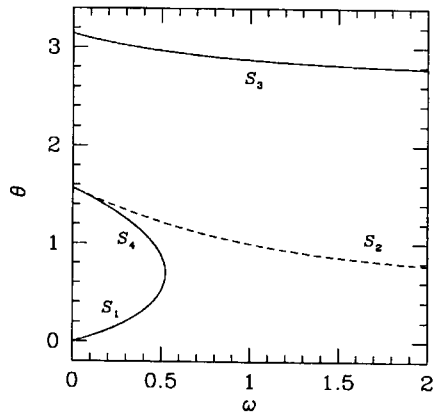

Figure 4. Bifurcation diagram for Equations (2) with $i = 30° = 0.524$ radians. As ω is increased, a saddle-node bifurcation occurs, reducing the number of Cassini states from four to two. Cassini state $\mathcal{S}_2$, denoted by the dashed curve, is located at $\phi = \pi$; all other branches are located at $\phi = 0$.

In Figure 4, we present the bifurcation diagram of the unperturbed system as the spin rate ω is varied. Equilibrium branches $\mathcal{S}_1$, $\mathcal{S}_3$, and $\mathcal{S}_4$ are located at $\phi = 0$ (so that $\xi = 1$ in Equation (4)), while for $\mathcal{S}_2$, $\phi = \pi$ ($\xi = -1$). Transcendental equations for the locations of these equilibria are given in Beletskii (1972). Near $\theta = \pi/2$, the branches labeled $\mathcal{S}_4$ and $\mathcal{S}_2$ remain a distance of $\Delta\phi = \pi$ apart in phase space. In this simple system, Cassini states $\mathcal{S}_1$, $\mathcal{S}_2$, and $\mathcal{S}_3$ are neutrally stable, while Cassini state $\mathcal{S}_4$ is of saddle-type stability.

As seen in Figure 4, Equations (2) possess either two, three, or four equilibrium points, depending on whether ω is larger, equal to, or smaller than a critical bifurcation value ω_{cr}. At $\omega = \omega_{cr}$, three equilibrium points exist as the system undergoes a saddle-node bifurcation (Hale and Koçak, 1991). As ω is increased through ω_{cr} Cassini states $\mathcal{S}_1$ and $\mathcal{S}_4$ coalesce and disappear. The value of ω_{cr} only depends on the orbital inclination i, but lies in the range $0.5 \leqslant \omega_{cr} \leqslant 1$ for all $0 \leqslant i \leqslant \pi$, and $\omega_{cr} \to 1$ as $i \to 0$. For $i = 30°$, we find that $\omega_{cr} \simeq 0.52$ (see Gladman et al. (1996, Figure 4a) for more details).

For $\omega > \omega_{cr}$, two Cassini states exist, $\mathcal{S}_2$ and $\mathcal{S}_3$. State $\mathcal{S}_2$ is stable, with $\phi = \pi$, and an obliquity satisfying $\sin 2\theta = 2\omega \sin(\theta - i)$. For $\omega < \omega_{cr}$, four Cassini states exist. In particular, Cassini state $\mathcal{S}_1$ exists and is stable, with $\phi = 0$, and an obliquity satisfying $\sin 2\theta = 2\omega \sin(\theta + i)$.

Because phase space is compact and two-dimensional, and the unperturbed system is conservative, almost all trajectories lie on closed, periodic orbits (the remaining solutions are asymptotic to the saddle-type equilibrium point $\mathcal{S}_4$ and of zero measure). In Figure 5 we show examples of the phase space of Equations (2) when there exist either two or four equilibrium points. Although the phase space is topologically equivalent to the surface of a sphere, we puncture this space

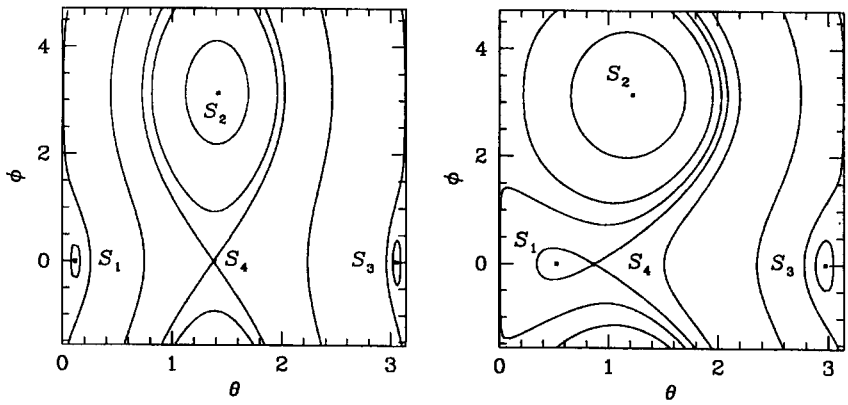

(a) $(\omega, i) = (0.2, 30°)$; (b) $(\omega, i) = (0.5, 30°)$;

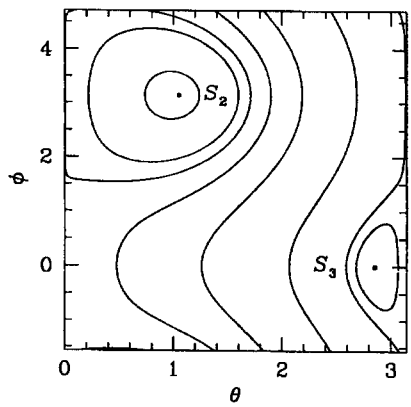

(c) $(\omega, i) = (1.0, 30°)$;

Figure 5. Phase portrait of Equations (2). The equilibrium points are marked and labeled $\mathcal{S}_1 - \mathcal{S}_4$. The phase space can be compared with the bifurcation diagram shown in Figure 4 to gain better understanding of the structure of Equations (2) as ω varies. Note that Figures (a) and (b) are topologically equivalent when viewed on the spherical phase space.

at the north and south poles ($\theta = 0, \pi$), and then flatten out this surface to represent it here.

For $\varepsilon = 0$, the phase space of the system is simple and well understood. However, because of the structural instability of the unperturbed system, these periodic solutions which fill phase space will in general cease to exist for $\varepsilon \neq 0$. Indeed, we find that the global limit cycle bears little resemblance to the trajectories of Equations (2).

4. Origins of the Limit Cycle

4.1. ω = CONSTANT

To understand the presence of the limit cycle of Equations (1) shown in Figure 3, we might expect to perform a small ε expansion starting with Equations (2). This strategy turns out to be inappropriate, however, because the limit cycle passes through a region of phase space which involves small values of ω (cf. Figure 3). This has the consequence that the term $-(\varepsilon\gamma \sin\theta)/\omega$ in Equation (1b), which is omitted in Equations (2), is not small over all portions of the limit cycle, and hence should not be neglected. Equation (1a), however, contains no such singularity, and so we are led to analyze the following system instead of Equations (2):

$$\dot{\omega} = 0, \tag{5a}$$

$$\dot{\theta} = \sin i \sin\phi + \varepsilon \sin\theta \left\{ \frac{\cos\theta}{2} - \frac{\gamma}{\omega} \right\}, \tag{5b}$$

$$\dot{\phi} = \sin i \frac{\cos\theta}{\sin\theta} \cos\phi + \cos i - \frac{\cos\theta}{\omega}, \tag{5c}$$

which we refer to as the *reduced* system. Thus we have again reduced Equations (1) from three to two dimensions, but have retained the effects of the ε/ω singularity of Equation (1b). However, we note that the reduced system is no longer conservative, and that it has two fixed parameters: γ and ω.

For $\varepsilon = 0.1$, $i = 30°$, and $\gamma = 0.56$, the bifurcation diagram of Equations (5) is shown in Figure 6. The spin rate ω, which is constant in the reduced system, is used as the bifurcation parameter. As in the unperturbed system, we identify four branches of equilibria, labeled as $\mathcal{R}_1$ through $\mathcal{R}_4$ as shown in the figure. $\mathcal{R}_1$ and $\mathcal{R}_2$ correspond to asymptotically stable fixed points of Equations (5). $\mathcal{R}_4$ is a branch of saddle points, while $\mathcal{R}_3$, located near $\theta = \pi$, is composed of asymptotically unstable foci.

Not surprisingly, for $\omega \gg \mathcal{O}(\varepsilon)$, where the ε/ω terms are small, the bifurcation diagram of the reduced system is almost identical to that of the unperturbed system (cf. Figures 4 and 6). In particular there exists a saddle-node bifurcation near ω_{cr}. However, for:

$$\omega = \mathcal{O}\left(\frac{\varepsilon\gamma}{\sin i}\right),$$

a fundamental difference between the bifurcation diagrams of these two systems is observed. In the reduced system, a second saddle-node bifurcation occurs between $\mathcal{R}_2$ and $\mathcal{R}_4$ (point P in Figure 6) *which has no counterpart in the unperturbed system*. In contrast, as $\omega \to 0$ in the unperturbed system, the equilibrium branches $\mathcal{S}_2$ and $\mathcal{S}_4$ remain a distance of $\phi = \pi$ apart in phase space.

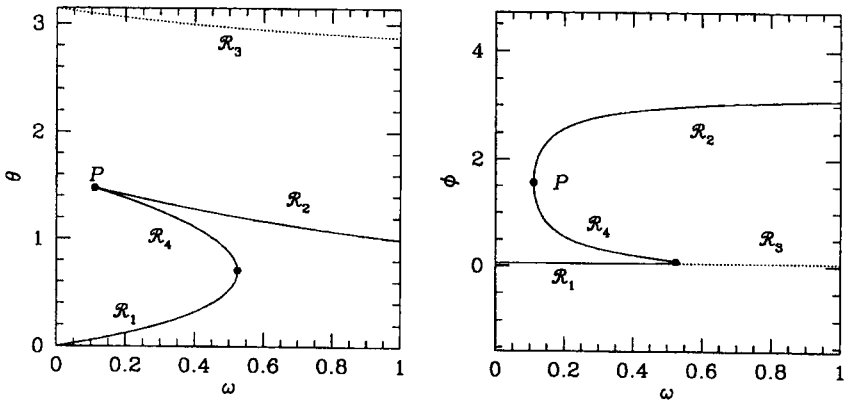

Figure 6. Bifurcation diagram of the reduced system; $\varepsilon = 0.1$, $i = 30°$, $\gamma = 0.56$. The saddle-node bifurcations are marked in both figures. Point P marks the saddle-node bifurcation between branches $\mathcal{R}_2$ and $\mathcal{R}_4$, a feature which is absent from the unperturbed system, cf. Figure 4. Note that for small ω, $\mathcal{R}_1$ and $\mathcal{R}_3$ are almost coincident in the $\omega - \phi$ projection. However, when viewed in $\omega - \theta$ space, these equilibrium branches are approximately a distance of π apart. The cusp-like appearance of the bifurcation curves is only an artifact of these two particular orthogonal projections.

4.2. ORIGINAL EQUATIONS

We can view the behavior of the original equations as occurring on two time scales: the reduced system, given by Equations (5), on a fast time scale, supplemented by a slow drift in ω (since $\dot{\omega} = \mathcal{O}(\varepsilon)$). In the reduced system we have simply set $\dot{\omega} = 0$ which, according to Equation (1a), requires:

$$\omega = 2\frac{\gamma \cos\theta}{1 + \cos^2\theta}, \tag{6}$$

which represents a two-dimensional surface in three-dimensional phase space. However, because Equation (6) is independent of ϕ, this surface, when projected onto the $\omega - \theta$ plane, is seen as a one-dimensional curve, which we also refer to as the $\dot{\omega}$ nullcline.

Comparing Equations (1) and (5) we see that the intersections of the $\dot{\omega}$ nullcline and the bifurcation diagram of the reduced system (cf. Figure 6) result in equilibrium points of the original equations. This requirement corresponds to simultaneously demanding the equilibrium of the spin pole location as well as the spin rate. By overlaying these two curves (as seen in the $\omega - \theta$ plane) we can graphically determine the equilibrium points of Equations (1). Equilibrium points of the original equations are also equilibrium points of the reduced system, but not conversely. In Figure 7 we show diagrams leading to the equilibrium point structure of the original equations for three values of γ.

On the $\dot{\omega}$ nullcline, as θ monotonically increases, ω monotonically decreases (cf. Equation (6)). As $\theta \to 0$, $\omega \to \gamma$, and as $\omega \to 0$, $\theta \to \frac{\pi}{2}$. Note that this implies

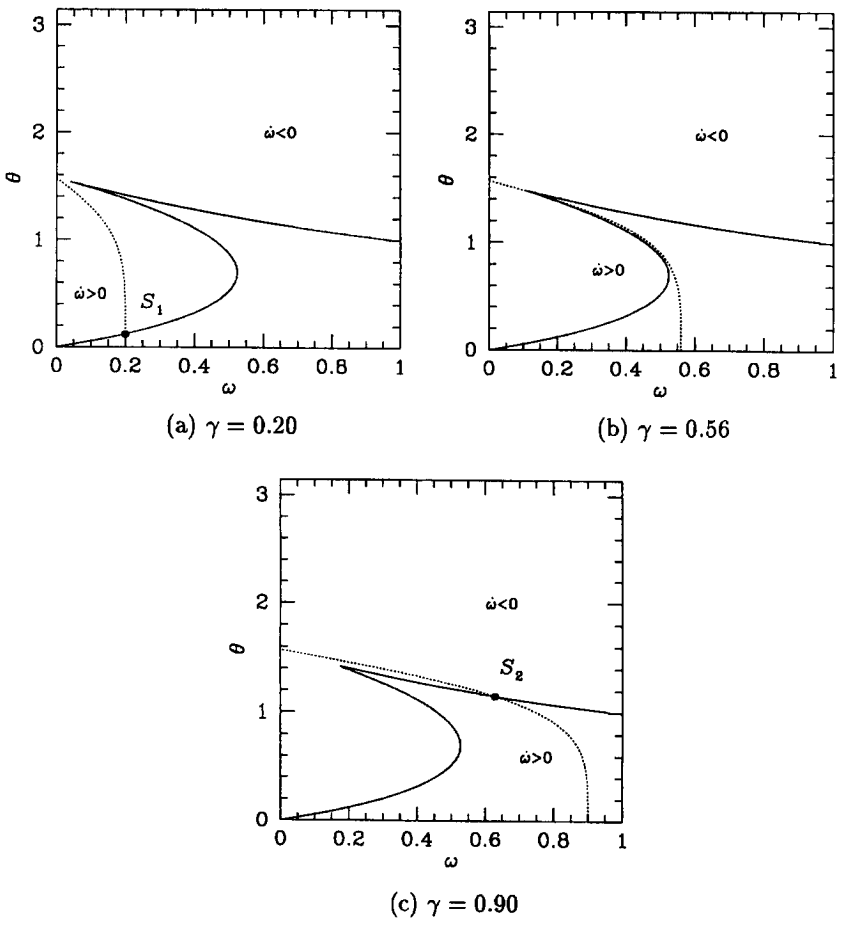

Figure 7. Nullclines: $\varepsilon = 0.1$, $i = 30°$. The bifurcation diagram of the reduced system, Figure 6, is shown as the solid line while the surface $\dot{\omega} = 0$, Equation (6), is represented by the dotted line. In the region for which $\dot{\omega} > 0$, solutions drift to the right; in the region $\dot{\omega} < 0$ solutions drift to the left (when projected in the $\omega - \theta$ plane). Intersections of these two curves indicate equilibria of the original system and are marked with the corresponding Cassini state.

that equilibrium solutions for an axisymmetric satellite *do not* correspond to synchronous rotation. Rather, all equilibrium states are subsynchronous; although for γ small the equilibrium states are only very slightly sub-synchronous (Figure 7a).

When viewed in the $\omega - \theta$ plane, trajectories that exist to the right and above the line $\dot{\omega} = 0$ are driven downwards in ω (in this region $\dot{\omega} < 0$) while trajectories to the left and below this line drift to the right ($\dot{\omega} > 0$). As a result, we can construct a trapping region (Guckenheimer and Holmes, 1983). All satellites spinning faster than synchronous ($\omega > \gamma$) are despun and subsequently cross into the region of phase space defined by $\omega \leqslant \gamma$. Consequently, the asymptotic behavior of all solutions is confined to this region in phase space.

For γ small, only one equilibrium point exists and can be identified with Cassini state $\mathcal{S}_1$ (Figure 7a). This fixed point is at low obliquity and approximately synchronous with:

$$\theta_{\text{eq}} \simeq \gamma \sin i, \qquad \phi_{\text{eq}} \simeq \frac{\varepsilon}{2}\gamma, \qquad \omega_{\text{eq}} \simeq \gamma.$$

The following argument shows that for γ sufficiently small no fixed point exists at high obliquity, near $\theta = 90°$. We see that at an equilibrium, substitution of the $\dot{\omega}$ nullcline, Equation (6), into Equation (5c) requires that:

$$\sin i \frac{\cos\theta}{\sin\theta}\cos\phi + \cos i = \frac{1+\cos^2\theta}{2\gamma}.$$

However, for small γ the right-hand-side is of $\mathcal{O}(1/\gamma)$, while for high obliquity the left-hand-side is of $\mathcal{O}(1)$. Clearly, this equation cannot be satisfied for sufficiently small γ; for low inclination and high obliquity, this transition is obviously near $\gamma = 1/2$.

For γ larger than some critical value (discussed below), we again find that there exists only one equilibrium point with:

$$\theta_{\text{eq}} \simeq i, \qquad \phi_{\text{eq}} \simeq \pi - \frac{\varepsilon}{2\cos i}, \qquad \omega_{\text{eq}} \simeq 2\gamma\frac{\cos i}{1+\cos^2 i}.$$

This fixed point can be identified with Cassini state $\mathcal{S}_2$.

However, in an intermediate range of γ, there exists the possibility of one, two, or three equilibrium points, depending on the topology of the $\dot{\omega} = 0$ nullcline and the bifurcation diagram of the reduced system. In general, we again vary γ while holding ε and i fixed. For values of ε and i for which three equilibrium points exist, we find that two fixed points are born through a saddle-node bifurcation as γ is increased through some critical value, ($\gamma = 0.536$ for $\varepsilon = 0.1$, $i = 30°$, cf. Figure 8). As γ is further increased, to $\gamma = 0.551$ for these parameters, the system undergoes a second saddle-node bifurcation, at which point two equilibria coalesce, leaving only the single branch of equilibria found above for γ sufficiently large.

We find that these saddle-node bifurcations occur solely on $\mathcal{R}_4$, the branch of unstable equilibria in the reduced system. When viewed in the $\omega - \theta$ projection, the saddle-node bifurcations exhibited by the full system are a result of tangencies between the $\dot{\omega} = 0$ surface and the curve of equilibria of the reduced system. However, unlike the more familiar saddle-node bifurcation in two dimensions, in three and higher dimensions the bifurcating solutions need not occur as an unstable saddle and stable node. Instead, as in this case, *both* of the new equilibrium points can be unstable, due to the added dimension of the system.

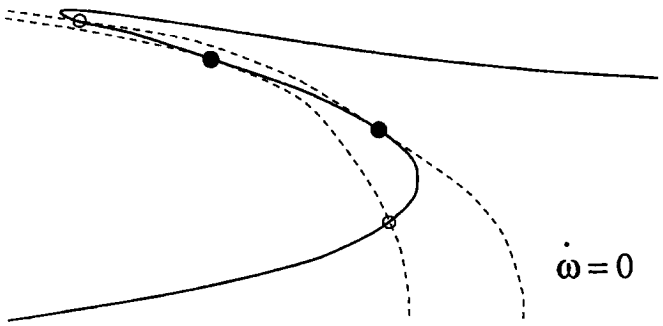

Figure 8. Representation of the occurrence of saddle-node bifurcations in the original system. The bifurcation diagram of the reduced system is shown as the solid curve, while the $\dot{\omega} = 0$ nullcline is shown dashed, in two key positions, each of which depicts a tangency leading to a saddle-node bifurcation in Equations (1), marked by the large filled dots. Additional hyperbolic equilibria are denoted by the smaller open circles. Note that this figure is only a cartoon, to be compared with Figure 7.

4.3. STABILITY

In the original equations, equilibria correspond to intersections of the surface defined by $\dot{\omega} = 0$ and the bifurcation of the reduced system, on which $\dot{\theta} = 0$ and $\dot{\phi} = 0$. Consequently, for equilibrium points of the original system we can easily identify the corresponding branch of equilibria in the reduced system.

In the reduced system, because ω is constant, the stability of the equilibria is straightforward: branches $\mathcal{R}_1$ and $\mathcal{R}_2$ are composed of stable equilibria while $\mathcal{R}_4$ is unstable. We disregard $\mathcal{R}_3$, on which no equilibria of Equations (1) exist ($\dot{\omega} = 0$ requires that $\theta < \pi/2$, while for $\mathcal{R}_3$, $\theta \sim \pi$); physically no equilibrium points of the original equations exist on $\mathcal{R}_3$ because tides always reduce the spin rate of retrograde satellites.

We attempt to characterize the stability of the original system by the behavior of the reduced system. Although the stability of equilibria in the reduced system is exact, such results only approximately carry over to the original system. Recall that the reduced system is essentially obtained by holding the spin rate ω constant in the original system. When analyzing the stability of equilibria in the original system, the state dependence of ω can slightly alter the stability of the equilibria.

The evolution of the state variable ω, according to Equation (1a), is toward the plane defined by $\dot{\omega} = 0$. Thus, as a lowest order approximation, the equilibria of the original equations will be stable if they lie on either $\mathcal{R}_1$ or $\mathcal{R}_2$, and unstable otherwise. Because of the singular term $\varepsilon\gamma/\omega$, these approximate stability results do not become exact, even in the limit $\varepsilon \to 0$.

For equilibria of Equations (1), we expect a change of stability to occur approximately when the equilibrium point of the original system passes through a change in stability in the reduced system, which occur at the saddle-node bifurcations of the

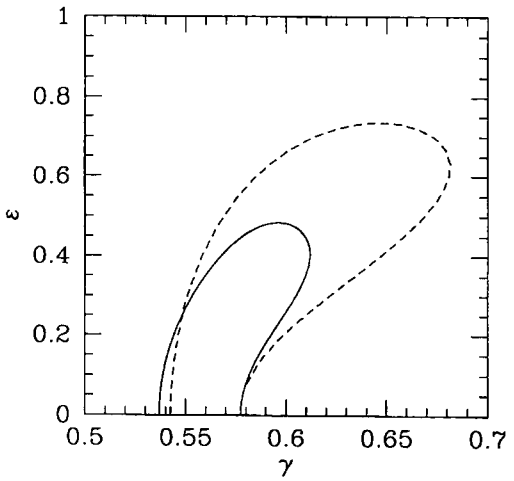

Figure 9. Bifurcation set of Equations (1) shown in $\varepsilon - \gamma$ space for $i = 30°$. The lowest order approximation to the stability change (as calculated in Appendix 5) is shown dashed. In contrast, the exact numerical stability change (on which occurs a Hopf bifurcation) is shown as the solid line. The exact results were obtained with the numerical continuation program AUTO (Doedel, 1986). The limit cycle exists within the region defined by the Hopf bifurcation. Note the expanded scale of the γ-axis.

reduced system. We emphasize that saddle-node bifurcations of the reduced system *do not* coincide with the saddle-node bifurcations in the original system, which were described in the previous section. Saddle-node bifurcations of the reduced system are seen as vertical tangencies in Figure 6, while saddle-node bifurcations in the original equations correspond to tangencies between the bifurcation diagram of the reduced system and the curve defined by $\dot{\omega} = 0$ (cf., Figure 8).

In Appendix A, we evaluate this approximate stability boundary based on the reduced system. In Figure 9, we show that this criterion, while not exact, does provide a very good approximation to the exact stability change of the equilibria obtained numerically. The exact stability boundaries in this case correspond to Hopf bifurcations in Equations (1). We expect the dynamical behavior of ω in Equations (1) to alter the local dynamics in the neighborhood of equilibria, and clearly this departure will increase for larger ε (Figure 9).

We are now in a position to explain the results seen in Figure 2 in terms of intersecting nullclines. At $\gamma = 0.536$, the $\dot{\omega} = 0$ nullcline first touches the $\mathcal{R}_4$ branch near $\theta = 1.25$, giving rise to a saddle-node bifurcation and spawning two unstable equilibrium points. Then the stable $\mathcal{R}_1$ solution reaches the low obliquity saddle-node bifurcation in the reduced system, corresponding roughly to the Hopf bifurcation and accompanying stability change at $\gamma = 0.538$; this now unstable equilibrium point lies on $\mathcal{R}_4$. Then two of the three solutions on the unstable branch, including the point formerly on $\mathcal{R}_1$, move together and 'annihilate' at $\gamma = 0.551$ and $\theta = 0.85$. Finally, the remaining solution on $\mathcal{R}_4$ undergoes a Hopf bifurcation

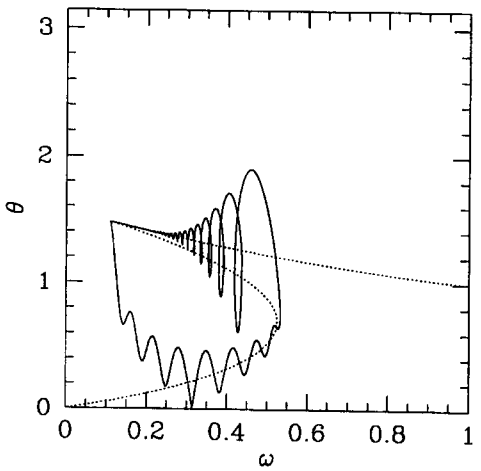

Figure 10. Limit Cycle vs. Constant ω Bifurcation Diagram ($\varepsilon = 0.1$, $\gamma = 0.56$, $i = 30°$). The dotted line represents the bifurcation diagram of Equations (5).

at $\gamma = 0.582$, related to crossing the high-obliquity saddle-node bifurcation in the reduced system, at which point it becomes stable as γ is further increased. This lone equilibrium point becomes the stable $\mathcal{R}_2$ solution for large γ.

Although the reduced system is also structurally unstable (because $\dot{\omega} = 0$), not only does it explain the bifurcation diagram of the original system, but it serves as a useful template for the dynamics of the global limit cycle. In Figure 10 we overlay the limit cycle on the bifurcation diagram of the reduced system; the limit cycle undergoes jumps as the trajectory traverses the saddle-node bifurcations of the reduced system. The reduced system may be thought of as an outer expansion (Bender and Orszag, 1978). During the jump the assumption $\dot{\omega} = 0$ is invalid: the behavior during the jump would be given by an inner expansion or boundary layer which we have not found. In addition, because the reduced system is dissipative, after the jump the limit cycle is reattracted to the equilibria of the reduced system. This phenomena is reminiscent of the analysis of Holden and Erneux (1993a; 1993b) on the slow passage through a Hopf bifurcation.

Numerically, we find that the global limit cycle grows from the Hopf bifurcation (cf. Figure 9), which results in a small amplitude, period one limit cycle. This local limit cycle undergoes a period doubling sequence which ultimately results in a Rössler-like attractor (Lichtenberg and Lieberman, 1992). However, this chaotic feature remains confined to a neighborhood of a fixed point. As the parameters are further tuned, the chaotic attractor suddenly breaks out into the global limit cycle. This transition is reminiscent of Canard-type solutions (Eckhaus, 1983) and is beyond the scope of this paper.

Clearly, the existence of the limit cycle is not based solely on the structure of the reduced system but on the interaction between the bifurcation diagram of this

system and the $\dot{\omega} = 0$ surface. However, if no stable equilibrium points exist, almost all solutions must be attracted to some non-trivial limit set (recall that all solutions are driven to a subsynchronous state). For $\varepsilon \ll 1$, $i = 30°$ and $\gamma \subset (0.538, 0.582)$ (cf. Figure 9), all intersections of the two nullclines lie along $\mathcal{R}_4$, the unstable branch of the reduced system (cf. Figure 7b), and the global limit cycle exists. Note that if ε is large (for example in Figure 9, $\varepsilon > 0.8$), we expect no bifurcations of above form; the 'S' shaped bifurcation curve of the reduced system (as seen in Figure 6) straightens out, so that no saddle node bifurcations exist in the reduced system.

4.4. LOW INCLINATION

If the nullclines intersect in such a way as to produce a stable equilibrium, we expect that solutions will be attracted to this point and no limit cycle will exist, although this is unproven. Indeed, for $\varepsilon = 0.1$ and $i = 30°$ this occurs for all γ outside the thin region in which the limit cycle exists. In addition, for lower values of inclination ($i <\sim 20°$), we find that as γ is varied the bifurcations identified above still occur, although their sequence is varied. In fact, we find that the high-obliquity stability change occurs before (in γ) the corresponding low-obliquity bifurcation. This would correspond to switching the order of the Hopf bifurcations (in γ) as seen in Figure 2b. In such a situation, the equilibrium point that lies on $\mathcal{R}_2$ coexists with the point on $\mathcal{R}_1$, which implies that at least one stable equilibrium point exists for all γ, and an intermediate range of γ contains two stable equilibria. Consequently, the limit cycle does not persist for small inclination; within the small range of γ in which two stable equilibria exist, the asymptotic behavior of the system depends on the initial conditions.

5. Conclusions

In standard perturbation analysis a reduced system is found by setting the small parameter $\varepsilon = 0$. However, one must be careful to analyze the form of the perturbation term. In Equations (1) the perturbation contains terms that behave like ε/ω. Thus, for fixed ε as $\omega \to 0$ the perturbation grows without bound and the perturbation approach is invalidated.

We have shown that the introduction of such a term dramatically alters the behavior of the reduced system (with ω held fixed) and therefore the conclusions that can be drawn about the original system. Specifically, the terms result in an additional saddle-node bifurcation in the reduced system and the limit cycle which exists in the original system is found to be understandable as a relaxation oscillation. Using a geometrical analysis, we have determined conditions on the system for the existence of a limit cycle.

Although such a limit cycle could, in theory, have existed at one time during an axisymmetric satellite's tidal evolution, in this study when $\gamma \simeq 0.56$ and Cassini

state $\mathcal{S}_1$ ceased to be stable, torques due to the satellite's permanent triaxial figure would probably have stabilized the spin rate at the synchronous value ($\omega = \gamma$) and thus prevented its development (Gladman et al., 1996). We have shown through some limited numerical experiments that even triaxial satellites can exhibit the limit cycle behavior, although only at unphysically high inclination under large tidal dissipation (e.g., Io at $i = 30°$). However, even for slow tidal dissipation, a satellite in the appropriate γ regime might be removed from synchronous rotation (by a collision for example), at which point the effects of a triaxial component average out and the dynamics illustrated here are valid until synchronous rotation is again transited.

The dynamical phenomena seen in the equations studied here can be understood in terms of the reduced system given in Equations (5). Specifically, the evolution of the original system can be decomposed into the behavior of the reduced system on a fast timescale, coupled with a slow drift in ω. The Hopf bifurcations which give rise to the global limit cycle (cf. Figure 3) are related to the saddle-node bifurcations in this reduced system. The saddle-node bifurcations of the original system are seen as tangencies between the bifurcation diagram of the reduced system (cf. Figure 7) and the surface on which $\dot{\omega} = 0$.

Although the global limit cycle exists only for unphysically high inclinations, the geometric methods used to examine its existence are valid for more realistic parameter values. Again, although the limit cycle would no longer exist, the dynamical behavior of such a system would be dramatically different from the unperturbed system. We conclude that it is in general perilous to interpret the global behavior of a dissipatively perturbed Hamiltonian system as simply a slightly modified version of the original system. The perturbed system can have global dynamics completely absent from the original system.

Appendix A. Calculation of Approximate Stability Regions

In this appendix we calculate the approximate bifurcation set based on the interaction of the reduced system with the $\dot{\omega} = 0$ nullcline.

As stated in the text, equilibrium points of Equations (1) are exactly the intersections between the bifurcation diagram of the reduced system, Equations (5), and the surface defined by $\dot{\omega} = 0$, as γ is varied. As a result, and as a lowest order approximation, we expect that stability changes of the equilibrium points of the full system will correspond closely to the saddle node bifurcations in the reduced system.

This condition can be formulated explicitly by finding the location of a saddle node bifurcation in Equations (5), in terms of the parameters γ, ε, i, and ω, and

then requiring this point to satisfy $\dot{\omega} = 0$, *i.e.*, Equation (6). This procedure results in a single equation that must be satisfied by the parameters of the system. When satisfied, one might expect that there will exist a stability change of the equilibrium points of Equations (1).

Following this procedure, we find that equilibrium points of the reduced system satisfy the following sixth order polynomial in $\cos\theta$:

$$\begin{aligned} f(\omega, \cos\theta) &= (\varepsilon^2\omega^2)\cos^6\theta + (-4\varepsilon^2\omega\gamma)\cos^5\theta \\ &\quad +(-\varepsilon^2\omega^2 + 4\varepsilon^2\gamma^2 + 4)\cos^4\theta \\ &\quad + (4\varepsilon^2\omega\gamma - 8\omega\cos i)\cos^3\theta(4\omega^2 - 4\varepsilon^2\gamma^2 - 4)\cos^2\theta \\ &\quad +(8\omega\cos i)\cos\theta + (-4\omega^2\cos^2 i), \\ &= 0. \end{aligned} \tag{7}$$

The solutions of this equation lead to the bifurcation diagram of Figure 6. Taking the total derivative of this equation with respect to θ:

$$0 = \frac{\partial f}{\partial\theta} + \frac{\partial f}{\partial\omega}\frac{\mathrm{d}\omega}{\mathrm{d}\theta}.$$

At the saddle node bifurcation $\frac{\mathrm{d}\omega}{\mathrm{d}\theta} = 0$. Therefore, since f is smooth and non-singular:

$$\frac{\partial f}{\partial\theta} = 0. \tag{8}$$

Finally, requiring that the equilibrium point satisfy $\dot{\omega} = 0$ demands:

$$\omega = 2\frac{\gamma\cos\theta}{1 + \cos^2\theta}.$$

Substituting this value for ω in Equations (7) and (8), we find two equations for $\cos\theta$ and the parameters of the system that must simultaneously be satisfied. Finally, eliminating $\cos\theta$ from these equations yields one equation that determines the approximate location of the stability change of the equilibrium points of Equations (1), shown as the dotted line in Figure 9 for $i = 30°$.

Acknowledgements

The authors would like to thank Stan Peale of USCB for his thoughtful review which greatly improved the clarity of the paper. This work was supported by NASA Grant NAGW-544.

References

Beletskii, V. V.: 1972, Resonance rotation of celestial bodies and Cassini's laws. *Celestial Mechanics* **6**, 356–378.

Bender, Carl W. and Orszag, Steven A.: 1978, *Advanced Mathematical Methods for Scientists and Engineers*. McGraw-Hill, Inc., New York.

Doedel, Eusebius: 1986, AUTO: Software for continuation and bifurcation problems in ordinary differential equations. Applied mathematics reports, California Institute of Technology.

Eckhaus, Wiktor: 1983, Relaxation oscillations including a standard chase on french ducks. In: *Lecture Notes in Mathematics 985, Asymptotic Analysis II–Surveys and New Trends*, Springer-Verlag, New York, pp. 449–494.

Gladman, Brett J., Quinn, D. Dane, Nicholson, Phil and Rand, Richard H.: 1996, Synchronous locking of tidally evolving satellites. *Icarus* **122**, 166–192.

Guckenheimer, John and Holmes, Phillip J.: *Nonlinear Oscillations, Dynamical Systems, and Bifurcations of Vector Fields*. Applied Mathematical Sciences **42**. Springer-Verlag, New York.

Hale, Jack K. and Koçak, Hüseyin: 1991, *Dynamics and Bifurcations*. Springer-Verlag, New York.

Henrard, Jacques and Murigande, Charles: 1987, Colombo's top. *Celestial Mechanics* **40**, 345–366.

Holden, Lisa and Erneux, Thomas: 1993, Slow passage through a Hopf bifurcation: From oscillatory to steady state solutions. *SIAM Journal on Applied Mathematics* **53**(4), 1045–1058.

Holden, Lisa and Erneux, Thomas: 1993, Understanding bursting oscillations as periodic slow passages through bifurcation and limit points. *Journal of Mathematical Biology* **31**, 351–365.

Lichtenberg, Allen J. and Lieberman, Michael A.: 1992, *Regular and Chaotic Dynamics*. Applied Mathematical Sciences **38**. 2nd ed. Springer-Verlag, New York.

Peale, Stanton J.: 1969, Generalized Cassini's laws. *Astronomical Journal* **74**, 483–489.

Peale, Stanton J.: 1974, Possible histories of the obliquity of Mercury. *Astronomical Journal* **79**, 722–744.

Ward, William R.: 1975, Past orientation of the lunar spin axis. *Science* **189**, 377–379.